Satellite Characterization and Modeling of Dust Transport from the Copper River Valley, Alaska

Robert Velarde[1], Dr. Santiago Gassó[2]

The University of Texas at El Paso[1]
University of Maryland Baltimore County[2]

ABSTRACT

Katabatic winds from the Copper River Valley in Alaska deposit substantial quantities of dust into the Gulf of Alaska. The main thrust of this study was to better understand dust events in the Copper River Valley and subsequent biogeochemical impacts these events have in the Gulf of Alaska. A number of dust events detected by MODIS (Moderate Resolution Imaging Spectroradiometer) satellite in late October, 2009 were analyzed and correlated with HYSPLIT (Hybrid Single-Particle Lagrangian Integrated Trajectory) simulations. Transport distances, heights, and concentration values of fine sand (50 μm), silt (2 μm – 50 μm), and clay (< 2 μm) were estimated relative to these textural size classes. There was a large variance between HYSPLIT simulation results and actual wind dust events evident in MODIS images; thus, the resulting dust concentration variations over the Copper River Valley area were inconclusive. However, since few studies of this nature have been conducted in this area, this investigation can provide useful information for future phytoplankton propagation research in the Gulf of Alaska. The HYSPLIT simulation parameters employed in this study can also be applied to other high latitude studies.

1. Introduction

The Copper River originates northeast of Mt. Wrangell at the Copper Glacier and flows south towards the Gulf of Alaska (Figures 1a and 1b). It is approximately 462 km in length and 1.6 km wide with a slope of 2.3 m/km (≈ 1:435); and has a drainage basin of approximately 63,000 km^2 (Carrick, 1992 cited in Bowersox, 2002). Mountain ranges that surround the Copper River are the Talkeetna Mountains (west), the Alaska Range (north), and the Wrangell-St. Elias Mountains (east). Surface runoff from rainfall, snow melt, glacial melt, and wind are the erosive mechanisms by which river valleys can be altered over time. These mechanisms coupled with the Copper River Valley's high energy gradient can deliver high sediment loads. The high-flow period commences as rainfall and glacial melt increase runoff in late May or early June. This high-flow period extends through August. This is when most of the river's discharge occurs. Low-flow periods occur between November and April due to glacial freezing (Figure 2a).

For approximately 145 km, stream terraces and river bank areas along the Copper River Valley introduce dust downwind during these wind events. (Details of these dust source areas have not been field verified and should be viewed as only estimates for model simulation input.) Katabatic winds from the Copper River Valley in Alaska deposit substantial quantities of dust into the Gulf of Alaska. Katabatic winds are cold winds with negative buoyancy which drain along the valley walls to the valley floor. Horizontal temperature gradients caused by differential solar heating or longwave cooling cause a horizontal pressure gradient. Layers of less cooled air do not descend

all the way to the valley floor, but spread horizontally at their level of neutral buoyancy (Wallace and Hobbs, 2006).

In late October, 2009, dust events were detected by MODIS (Moderate Resolution Imaging Spectroradiometer) satellite. The MODIS images, which indicate dust trajectory patterns, were correlated with HYSPLIT (Hybrid Single-Particle Lagrangian Integrated Trajectory) simulations in order to estimate transport distances and heights of fine sand (50 μm), silt (2 μm – 50 μm), and clay (< 2 μm) particles. These soil particle size designations are categorized according to the United States Department of Agriculture (USDA) soil drainage classification system (USDA, 1997). Dust concentration values were also estimated relative to particle size and transport distance.

The overall scope of this study was to give us a better understanding of dust behavior patterns in the Gulf of Alaska and subsequent biogeochemical impacts these events have in the Gulf of Alaska. Ultimately, these findings can aid future phytoplankton growth pattern studies in the Gulf of Alaska. Few in-depth studies on dust suspension and biogeochemical cycling in this region have been undertaken. These results can also provide useful data for modeling similar events in highly defined terrain at high latitudes.

The highest percentage (85%) of textural size class was silt (2 -50 μm) (Clark and Kautz, 1990). The threshold at which clay size particles end and silt size particles begin is 2 μm according to the USDA (USDA, 1997). In terms of textural size class, clays and silts near the 2 μm size can contain potential nutrients for phytoplankton. Some areas of the Copper River Valley have an organic covering (Clark and Kautz, 1990). As to whether this organic layer affects phytoplankton adversely or favorably is unknown.

Dust and organic particles can introduce nutrients into the ocean via strong wind events. Ocean particles can be lithogenic or biogenic. Biogenic particles are composed of organic matter produced by organisms or shell material (calcium carbonate and opaline). Lithogenic particles are composed of silicate material from river runoff and atmospheric deposition. However, it is possible for all these components to be present in any given particulate sample. An average value for suspended particulate matter (SPM) has been estimated to be 75% organic matter, 14.3% carbonate shell material, 4.4% opal shell material, and 6.3% lithogenic material (Kuss and Kremling, 1999 cited in Eby, 2004). Metals can serve as micronutrients for phytoplankton (Eby, 2004). The Redfield ratio (introduced by oceanographer Alfred C. Redfield) is the ratio of carbon, nitrogen, and phosphorus in phytoplankton. Specifically, Redfield determined the largest ratios for open-ocean plankton corresponded to elements carbon, nitrogen, phosphorus, nitrogen, and iron (Kuss and Kremling, 1999 cited in Eby, 2004). The enrichment factor (EF) pertains to the concentration of metals in marine organisms versus metals in seawater (Eby, 2004). Four metals found in phytoplankton organic tissue with dominant EF concentration values are Fe, Zn, Pb, and Al (Libes, 1992 cited in Eby, 2004). Dissolved metals can be adsorbed onto particles composed of clay minerals, oxyhydroxides, particulate organic matter, and shell material (Eby, 2004).

2. Methodology

2.1 Image Selection

Dust events and high-flow periods were established by analytical inspection of MODIS HDF 250 m resolution visible images, LANDSAT satellite images, and river images during high-flow periods. A substantial quantity of satellite images were examined for the months of July, October, and November, 2009. Based on these observations, MODIS 250 m images that best depicted potential dust source areas and dust storm events along the Copper River Valley were selected for processing with HDFLook software.

2.2 Visible Imagery (GeoTiff) Generation

HDFLook was utilized to process MODIS HDF files and generate 250 m visible GeoTIFF images.

2.3 Estimating Dust Source Areas

The GeoTIFF images generated by HDFLook were imported (i.e., Add Image Overly) into Google Earth and oriented properly with respect to longitude and latitude coordinates for geospatial accuracy. MODIS images which clearly reveal dust events are infrequent; therefore, only two GeoTIFF images corresponding to different periods (July and October, 2009) were selected for area estimation. The July 12, 2009 GeoTIFF image shows the Copper River flowing during a high-flow period (Figure 2a). During the low-flow periods (between November and April) is when stream terraces are at maximum exposure and can potentially serve as dust sources. However, to what degree saturated soil and coarse sediment particles (e.g., gravel) impede suspension of fine particles (e.g., clay and silt, and fine sand) is unknown. Barring in-situ investigations, dust suspension estimates can be achieved with remote sensing techniques (e.g., MODIS) and by probing geotechnical literature such as the USDA soils report by Clark and Kautz (1990). The October 30, 2009 image shows the boundary limits of the dust plume flowing down the Copper River Valley (Figure 24). Finding potentially dust yielding source areas was a formidable undertaking since saturated soil is difficult to differentiate during dust events captured by satellite. Potential dust sources in stream terraces and river banks were estimated by inspecting LANDSAT and MODIS satellite images and drawing polygons over potential dust source areas via GEPath and MapTool 2 (areas were cross verified with GEPath and MapTool 2). Stream terraces are features formed from erosion of alluvial deposits by the Copper River (Figure 2b). GEPath interacts with Google Earth while MapTool 2 is an interactive online tool (http://www.zonums.com/gmaps/maptool.php). The approximated 565 km^2 of potential dust source area was the net result of the area bound by the limits of the dust plume, minus the boundary limits of the saturated Copper River, plus the sum of stream terraces (plume – river + terraces ≈ 565 km^2).

The USDA *Soil Survey of Copper River Area, Alaska* report by Clark and Kautz (1990) was utilized in this study. Valuable details such as coordinates of collected soil samples, soil properties, area descriptions, and particle-size distribution were provided in this USDA survey. Since the Gakona soil sample (number 441) obtained at 61° 44’ 00’’ latitude, 144° 53’ 00” longitude was closest to the Copper River and our study site, the Gakona soil sample was

selected as a proxy. The Gakona study site covers approximately 58 km^2 (14,228 acres) and is located approximately 50 km upstream of our study area. The Gakona soil sample is described as thin silty loess (aeolian sediment containing clay and silt held together loosely by calcium carbonate) mantle over clayey lacustrine (lake) deposits. The bulk density of oven dried material was reported to be 0.97 gcm^{-3}. The reported particle-size distributions of clay, silt, and sand were 5.7%, 85%, and 9.3%, respectively. Extractable bases in rank order were Ca, Mg, K, and Na. These values correspond to the one inch topsoil horizon. The topsoil horizon was covered by one inch of organic cover. As previously mentioned, this study site was estimated to have approximately 565 km^2 of potential dust source area. This includes stream terraces (typically called sandbars) along the Copper River. However, many of these stream terraces have coarse gravel on the top horizon from alluvial deposits which can hinder dust suspension during dust events. Exactly how soil moisture and vegetation affects dust suspension in this area is unknown; therefore, 565 km^2 is more likely an upper end limit, while 500 km^2 is more likely a lower end limit.

Soil in the stream terraces have been classified by the USDA as Gulkana (number 429) soil comprised of silty loess over sandy and gravelly alluvium. This is similar to the Gakona soil with the exception that the Gulkana soil contains gravel. Coarse sand and gravel particles can impede fine clay and silt particles from suspending readily during strong wind episodes. These stream terraces will not emit equivalent amounts of dust as unimpeded areas. Therefore, vertical mass flux (gm^{-2}) values for these stream terraces were roughly estimated.

2.4 Remote Sensing and MODIS Fundamentals

Lillesand et al. (2004) state that spectral sensitivity for the human eye approximately ranges between 0.39 to 0.75 μm, whereas red (R), green (G), and blue (B) correspond to 0.65 μm, 0.56 μm, and 0.47 μm wavelengths, respectively. Earth's heat energy can be sensed with thermal scanners at 3 to 5 μm and 8 to 14 μm. MODIS has 36 spectral bands ranging from 0.659 to 14.385 μm with a 12-bit radiometric sensitivity. MODIS has a 2-day repeat global coverage with a 250 m (bands 1-2), 500 m (bands 3-7), and 1000 m (bands 8-36) spatial resolution. The RGB color cube is defined by the brightness levels of each of the primary colors. For a display with 8-bit-per-pixel data encoding, the range of possible DNs (digital numbers) for each color component is 0 to 255. Therefore, there are 256^3 (16,777,216) possible combinations of red, green, and blue DNs that can be displayed.

2.5 HYSPLIT Fundamentals

Saltation occurs when vertical turbulent forces (velocity components) have nearly no effect on particle trajectory (Pye, 1987). Suspension occurs when the settling velocity of the particle is nearly insignificant relative to the friction velocity (Pye, 1987). Trajectory between saltation and suspension is affected by the inertia and settling velocity of the particle (Pye, 1987). Sand grains carried by wind rarely go above 1 m, whereas the average carrying height is approximately 10 cm (Bagnold, 1954). Sand grains begin to mobilize on the ground approximately at 5 ms^{-1} (Bagnold, 1954). The saltating-dominated zone generally extends from the surface up to 0.2 to 0.3 m (Fryrear and Saleh, 1993). Small haze and smoke particles can remain in suspension as these particles collide with dispersive air molecules and subsequently displace while defying gravity (Bagnold, 1954). Typical diameter values for fine wind-blown sand range between 0.3 to

0.15 mm, whereas the finest wind-blown sand is not less than 0.08 mm in diameter (Bagnold, 1954). Past dust deposition studies indicate that 50 μm is a good median grain diameter which characterizes most dust mixtures well (Goossens, 2005). Smaller particles are susceptible to transport and dispersal as dust by upward eddy currents (Bagnold, 1954).

Under typical wind storm conditions, the friction velocity (u_*) approximately ranges from 0.20 to 0.60 ms^{-1} involving deposit mostly made of loess sediment, particles greater than 500 μm will creep (roll), particles 70 to 500 μm will saltate, particles 70 to 100 μm will undergo modified saltation, particles 20 to 70 μm will undergo short-term suspension, and particles less than 20 μm will undergo long-term suspension (Pye, 1987) (Figure 3). Dust entrainment occurs above the mixing layer. The mixing layer is under the atmospheric boundary layer which normally ranges 1 to 2 km thick and occupies the bottom 10 or 20% of the troposphere. It has a capping inversion with the troposphere above (Wallace and Hobbs, 2006).

Equations used by HYSPLIT pertinent to suspension and saltation are the settling velocity equation (1) (Van der Hoven, 1968; Pye, 1987; Seinfeld and Pandis, 1998; Eby, 2004) and the Prandtl-von Kármán equation (2) which defines the slope of the logarithmic wind profile (Pye, 1987).

Stokes' law determines the settling velocity of a spherical particle:

$$u_s = \frac{g(\rho_p - \rho_a)D_P^2}{18\mu} \quad \text{(settling velocity)} \qquad (1)$$

(It should be noted that the slip correction factor C_c is factored in when small particles are considered. If D_p is greater than 10 μm, C_c is usually neglected (Seinfeld and Pandis, 1998). C_c is a function of the mean free path (λ) and particle diameter (D_p). The mean free path is the average distance traveled by a molecule before colliding with another molecule.)

u_s = settling velocity (cms^{-1})
D_p = the particle diameter (cm)
ρ_p = the particle density (gcm^{-3})
ρ_a = air density (0.001225 gcm^{-3})
g = the acceleration due to gravity (980.665 cms^{-2})
μ = the dynamic viscosity of the air (1.789×10^{-4} g $cm^{-1}s^{-1}$ for standard atmosphere at sea level)

The Prandtl-von Kármán equation determines the slope of the logarithmic wind profile:

$$U = \frac{u_*}{k} \ln \frac{z}{z_0} \qquad (2)$$

U = Wind velocity (ms^{-1}) at height z above the ground

u_* = Drag velocity (ms^{-1})

z = Height above surface (m)

k = Dimensionless von Karman constant of 0.4

z_0 = Roughness length is the height at which the velocity is zero (roughness length is related to the height of the roughness elements on the surface)

The roughness length (z_0) depends on surface cover (e.g., urban, trees, grass, crops, desert, water, snow, ice, etc.) and can range from 10 m (urban type cover) to 10^{-5} m (smooth ice cover) (Seinfeld and Pandis, 1998). The roughness length is approximately 1/30 the diameter of the surface particles (von Kármán, 1934; Prandtl, 1935; Bagnold, 1941 cited in Pye, 1987) or $z_0 \approx$ 1/30 the height of the roughness elements covering the surface (Seinfeld and Pandis, 1998). The drag velocity (u_*) is directly proportional to the rate of increase of wind velocity with respect to logarithmic height (Bagnold, 1954).

The threshold friction velocity (3) is the critical point at which saltation occurs:

$$u_{*_t} = A\sqrt{\frac{\rho_p - \rho_a}{\rho_a} gD} \quad \text{(threshold friction velocity)} \qquad (3)$$

The coefficient A is equal to 0.1 for particle friction Reynolds numbers (Re_p) greater than 3.5 (i.e., $Re_p > 3.5$). Reynolds number = velocity (u_*) x mean particle diameter (D) / kinematic viscosity of air (μ). Re_p is a numerical value which indicates how turbulent the flow is around the particle (Bagnold, 1954; Pye, 1987).

u_{*_t} = the threshold friction velocity (cms^{-1})
ρ_p = the particle density (gcm^{-3})
ρ_a = the air density (0.001225 gcm^{-3})
g = the acceleration due to gravity (980.665 cms^{-2})
D = the mean particle diameter (cm)

3. Model Setup

3.1 Meteorological Files

The resolution preset by the Global Data Assimilation System (GDAS) meteorological files was too large to properly model the Copper River Valley's airshed domain. Over scaling prevented katabatic events in the Copper River Valley from being analyzed properly. To model something the size of the Copper River Valley, a regional (1,000 km x 1,000 km x 10 km and 20 km resolution) domain scale should be sufficient. The mesoscale (urban) (100 x 100 x 5 km and 2 km resolution) domain scale may be too small for the Copper River Valley. However, for the Gulf of Alaska, a synoptic (3,000 x 3,000 x 20 km and 80 km resolution) domain scale should be adequate.

The Copper River Valley has complex terrain which can complicate simulations if the meteorological resolution cannot address this satisfactorily. The GDAS data lie on a 360 by 181

latitude-longitude grid with the lower corner (1, 1) set at (0W, 90S) and the upper-right corner (360, 181) set at (1W, 90N).

GDAS files utilized to analyze the Copper River Valley were *20091029_gdas0p5*, *20091030_gdas0p5*, and *20091031_gdas0p5*. Simulations were setup for 24-hour duration periods for October 29, 2009; October 30, 2009; and October 31, 2009. Meteorological fields contained in the GDAS archive (Table 4) can be viewed online (http://ready.arl.noaa.gov/gdas1.php).

3.2 Point Sources as Areas

The Copper River Valley study area was divided into four sectors to facilitate HYSPLIT input. However, it was not possible to input area sectors in polygon form into HYSPLIT; therefore, area sectors had to be represented by point sources with assigned circular areas. Another complication was that the Copper River Valley's airshed domain was too small (as mentioned previously) to properly analyze it with adequate resolution. These limitations yielded particle trajectories which did not correlate with wind flow patterns in the Copper River Valley. Consequently, a single point source representing the entire Copper River Valley airshed (565 km^2) was positioned in the Copper River Delta at 60.40 latitude, -144.98 longitude 10 m above sea-level for all simulations. Six vertical levels were set to define the concentration grid at 0, 100, 500, 1,000, 2,000, and 3,000 meters.

3.3 Emission Estimates

The HYSPLIT model utilizes a pre-processing dust storm program for the emission of PM10 which accesses a land-use file for any selected domain (Draxler et al., 2001). This selection can be done by either selecting the radio button "Enable the PM10 dust storm emission algorithm for desert landuse" under In-Line chemical CONVERSION MODULES (10) or setting ICHEM = 3 in the SETUP.CFG file. By making this selection, an emissions rate is computed when wind velocity exceeds the threshold friction velocity which is a function of surface roughness. Surface roughness is a function of surface geomorphology (soil properties). All simulations for this study were done under dry conditions. The flux (gm^{-2}) equation (4) below was used to make flux (F) estimates (Wetsphal et al., 1987 cited in Escudero et al., 2006).

$$F = 0.01u_*^4 \text{ = mass/area (gm}^{-2}\text{)} \quad (4)$$

$$u_* \text{ = friction velocity (ms}^{-1}\text{)}$$

These estimates were computed using values provided in the USDA soils report by Clark and Kautz (1990). The dry bulk density of the Gakona proxy sample was 0.97 gcm^{-3} while the percentages of clay, silt, and sand were 5.7%, 85%, and 9.3%, respectively (Clark and Kautz, 1990). Assigned densities for clay, slit, and sand were 2.50, 2.65, and 2.65 gcm^{-3}, respectively. Knowing that density is equal to mass/volume, the following equations were established:

$$V_t = (565 \times 10^6 \text{ m}^2) \times (1000 \times 10^{-6} \text{ m}) \text{ (total dry volume) (m}^3\text{)} \quad (5)$$

$$V_{clay} = V_t \text{ (5.7\%)} \quad (6)$$

$$V_{silt} = V_t \text{ (85\%)} \quad (7)$$

$$V_{sand}=V_t\ (9.3\%) \tag{8}$$

$$M_{clay} = \rho_d V_{clay} \tag{9}$$

$$M_{silt} = \rho_d V_{silt} \tag{10}$$

$$M_{sand} = \rho_d V_{sand} \tag{11}$$

$$M_{total} = M_{clay} + M_{silt} + M_{sand}\ \text{(total dry mass) (g)} \tag{12}$$

Estimating a dry volume (V_t) (5) by multiplying the estimated area (565 km^2) by a thickness of 1000 μm (coarse sand diameter), yields result values of mass proportions of flux.

$$1 = \frac{M_{clay}}{M_{total}} + \frac{M_{silt}}{M_{total}} + \frac{M_{sand}}{M_{total}} = C_{clay} + C_{silt} + C_{sand} \tag{13}$$

Specifically, C_{clay}, C_{silt}, and C_{sand} (14-16) are factors utilized as emissions input for HYSPLIT simulations as shown below.

$$C_{clay} = \frac{M_{clay}}{(F)(Area)} = \frac{g}{(gm^{-2})(m^2)} = 0.057 \tag{14}$$

$$C_{silt} = \frac{M_{silt}}{(F)(Area)} = \frac{g}{(gm^{-2})(m^2)} = 0.85 \tag{15}$$

$$C_{sand} = \frac{M_{sand}}{(F)(Area)} = \frac{g}{(gm^{-2})(m^2)} = 0.093 \tag{16}$$

These factors are emission source components for q_s ($\mu gm^{-2}h^{-1}$) in the LaGrangian Box Model (cell) equation (17) (Seinfeld and Pandis, 1998).

$$\frac{d}{dt}(c_s) = \frac{q_s}{H} + \cancel{kc_s} - \frac{v_s c_s}{H} + \cancel{\frac{(c_s^0 - c_s)}{\tau_r}} \tag{17}$$

The advection component (towards far right side of equation) is nullified since the species concentration (c_s) over the area of interest is considered equal to the upwind species concentration (c_s^0). Assuming the dust species is inert, the reaction rate (k) component is also nullified.

q_s = emitted rate of species ($\mu gm^{-2}h^{-1}$)

c_s = initial concentration of species (μgm^{-3})

c_s^0 = background concentration of species (μgm^{-3}) (The background concentration of species concentration corresponds to the airshed surrounding the study area.)

H = height of model box framework (m) (mixing layer height of airshed)

k = species reaction rate (percentage h^{-1})

v_s = dry deposition velocity of the species (mh^{-1})

τ_r = residence time of air over the area of interest (h)

4. Results and Discussion

The images displayed in the following pages were selected on the basis of chronology, dust deposition area at sea-level (on the ocean surface), potential atmospheric conditions, and particle size. The time periods pertaining to result figures (Figures 4-21) fall between 0400 and 2000 UTC with the exception of the HYSPLIT particle plots (Figure 7, 13, and 19) which correspond to 2100 UTC. A summary of distance, height, and concentration results are listed in Tables 1-3.

4.1 Sea Level Pressure and Wind Velocity over the Gulf of Alaska

Strong winds in Alaskan valleys were investigated via satellite infrared imagery by Marvill and Jayaweera (1975). Their studies were conducted along a southeasterly transect (Tanana River) approximately 190 km north of the Copper River Valley. Marvill and Jayaweera (1975) concluded strong valley winds correlated well with pressure gradients and the Tenana Valley slope (~1:1000), whereas light winds were parallel to isobars. Specifically, wind gusts were recorded in the Tenana Valley near the Big Delta (elevation 335 m) at 45 kt (23 ms^{-1}) with a temperature reading of -10 °F (-23 °C). Northway (161 km away at elevation 520 m) had a temperature reading of -45 °F (-43 °C) without wind gusts. Fairbanks, which is not exposed to these valley winds, recorded winds from the east to southeast at 35 kt (18 ms^{-1}) at approximately 900 mb (1, 200 m).

Between October 29, 2009 and October 31, 2009, low mean sea-level pressures (995 mb) and low mean wind velocities (4-6 ms^{-1}) were consistent southeast of the Copper River Valley (Figures 26 – 31). The highest mean wind velocities (15-20 ms^{-1}) were in close proximity to the highest mean sea-level temperatures (13-16 °C) south of the low pressure systems (Figures 27, 29, 31, and 32). Mean sea-level temperatures were consistent between October 29, 2009 and October 31, 2009 (Figure 32). Northeasterly (flowing from northwest) mean wind velocities near the Copper River Delta ranged between 7 and 9 ms^{-1}. These sea-level pressure, temperature, and velocity values are daily averages and do not necessarily depict exact meteorological conditions in the MODIS images (Figures 22, 24, and 25).

4.2 Dust event on October 29, 2009 (Julian Date 302)

High concentration (gm^{-2}) values occur at 0400 UTC at the 165 km mark since this is near the dust source (Figure 4). Concentration values for all particles sizes diminish uniformly with respect to distance and time (Figure 5). An initial radical rate drop in concentration for all particles occurs before the 200 km mark (Figure 5). Concentration values for all particles sizes reach their minimum values between 500 and 650 km (Figure 5). The uniform stratified appearance may be attributable to stable and layered flow in the atmosphere (Figure 5). The dust deposition area at sea-level remains clustered approximately 482 km southwest of the Copper River Valley (Figure 6) at 1200 UTC. The particle cross-section approximately 506 km from the source area indicates 2 μm particles suspended to approximately 5 km AGL (above ground level) (Figure 7). The dust deposition area at sea-level dispersed some but remained intact

approximately 506 km southwest of the source area at 2000 UTC (Figure 8). The concentrations values reached a minimum at approximately the 500 km mark (Figure 5). The dust deposition area for this time period was the most discrete (isolated from coastline terrain). Particles of 2 μm, 0.5 μm, and 0.1 μm size hold fairly stable concentration values up to 3 km AGL, whereas the 50 μm particle size concentration value approaches 0 gm^{-2} at approximately 2 km AGL (Figure 9).

4.3 Dust event on October 30, 2009 (Julian Date 303)

The dust deposition area at 0400 UTC was slightly more dispersed than the previous 24 hours. High concentration values (gm^{-2}) remained high at 200 km (as expected) since this occurs near the dust source (Figure 10). Concentration values for 2 μm, 0.5 μm, and 0.1 μm particles sizes diminish uniformly with respect to distance and time (Figure 11). An initial moderate rate drop in concentration for all particles occurs before the 200 km mark, but the concentration rate drop for the 50 μm particle becomes radical near the 375 km mark (Figure 11). The 50 μm particle's concentration rate drop is attributable to its size and assigned density (2.65 gcm^{-3}). Concentration values for all particles sizes reach their minimum values between 600 and 700 km (Figure 11). The dust deposition area at sea-level intrudes coastline terrain approximately 491 km southwest of the Copper River Valley (Figure 12) at 1200 UTC. The particle cross-section approximately 661 km from the source area indicates 2 μm particles suspended to approximately 10 km AGL (above ground level) (Figure 13). (The top of model was set to 10 km.) The dust deposition area at sea-level fragmented between 500 and 661 km southwest of the source area at 2000 UTC (Figure 14). Particles of 2 μm, 0.5 μm, and 0.1 μm size hold stable concentration values up to 3 km AGL, except the concentration of the 50 μm particle size radically approaches 0 gm^{-2} at approximately 1 km AGL (Figure 15).

4.4 Dust event on October 31, 2009 (Julian Date 304)

The dust deposition area was less dispersed and had the highest concentration values at 0400 UTC than the previous 48 hours. Since little dispersion took place, high concentration values (gm^{-2}) occurred near the dust source at the 101 km mark (Figure 16). Concentration values for 2 μm, 0.5 μm, and 0.1 μm particles sizes diminish uniformly with respect to distance and time near the 200 km mark (Figure 17). An initial moderate rate drop in concentration for all particles occurs before the 150 km mark; however, the rate drop in concentration becomes unstable at approximately the 175 km mark and radical for the 50 μm particle at approximately the 190 km mark (Figure 17). The 50 μm particle's concentration rate drop is attributable to its size and assigned density (2.65 gcm^{-3}). Concentration values for 2 μm, 0.5 μm, and 0.1 μm sizes reach their minimum values approximately between 130 and 210 km (Figure 17). The dust deposition area is approximately 104 km south of the Copper River Valley (Figure 18) at 1200 UTC. The particle cross-section approximately 104 km from the source area indicates 2 μm particles suspended to approximately 8 km AGL (above ground level) (Figure 19). The dust deposition area at sea-level dispersed some but mobilized little approximately 104 km from the source area at 2000 UTC (Figure 20). Since clouds can be reflective while remaining colder than ambient air, clouds can act as a lid and impede particle diffusion (Figure 25). Particles of 2 μm, 0.5 μm, and 0.1 μm size hold stable concentration values up to 3 km AGL, while the concentration of the 50 μm particle size approaches 0 gm^{-2} at approximately 2 km AGL (Figure 21).

4.5 Discriminating Atmospheric Dust

Aside from observing dust events in RGB satellite images, MODIS makes it possible to observe the earth's land, ocean, and atmosphere in the visible and infrared regions of the electromagnetic spectrum (Ackerman, 1998). Thermal IR (infrared) is particularly useful since atmospheric bodies such as clouds can be reflective in the visible regions of the spectrum, but colder than its surroundings when observed in thermal IR (Frey et al., 2008). By differentiating signals for individual spectral bands, contrasts of atmospheric bodies can be defined (Frey et al., 2008). Dust can be detected utilizing MODIS thermal IR bands 20, 30, 31, and 32 (Hao and Qu, 2007). An aerosol optical thickness (AOT) of 550 nm has been found to be relative to the brightness temperature of MODIS bands 20, 30, 31, and 32 (Hao and Qu, 2007). Moreover, brightness temperature differences between wavelengths 3.7 μm (band 20) and 12 μm (band 32), and wavelengths 11 μm (band 31) and 12 μm (band 32) were found to be sensitive to dust storms (Ackerman, 1998; Hao and Qu, 2007). Based on these findings, the October 19, 2009 MODIS HDF file was processed by MATLAB utilizing hdftool to generate a thermal IR grayscale image (Figure 23). A grayscale image is essentially a data matrix whose values represent intensities within some range and is generated by utilizing the "imagesc" and "colormap" MATLAB commands to manipulate bands. GeoTiff images for October 20, 2009 and October 21, 2009 were generated by HDFLook (Figures 22, 24, and 25). Figure 25 shows that a dust event can be concealed by clouds.

5. Conclusions

Obtaining satellite images which reveal actual dust events without cloud cover is invaluable. Research scientists seek to find satellite images in chronological order over a span of several days. This would help conduct computer simulations over a longer period of time which would subsequently yield more representative results.

Since the Copper River Valley domain is smaller than the model's meteorological resolution, over scaling prevents katabatic events in the Copper River Valley from being analyzed properly. The Copper River Valley has complex terrain which can complicate simulations if the meteorological resolution cannot address this satisfactorily.

Moreover, potential dust source areas had to be approximated by strategically locating single point sources with an assigned area (km^2). These point sources with an assigned area do not represent actual terrain boundaries well.

Therefore, resulting dust concentration variations over the Copper River Valley area should be considered inconclusive for this study. Notwithstanding the disadvantages mentioned above, these simulations can help modelers and field practitioners better understand investigative research in their respective areas of study. Also, dust event HYSPLIT simulation parameters for arid environments can be applied in high latitude regions.

6. Acknowledgements

I would like to extend my gratitude to scientists Dr. Santiago Gasso, Dr. Ali Tokay, and Dr. Jeffrey B. Halverson for sharing their knowledge. I offer my special thanks to Valerie Casasanto for all her hard work and attention she gave to the interns. I also thank all the people at NASA GSFC that made this internship possible.

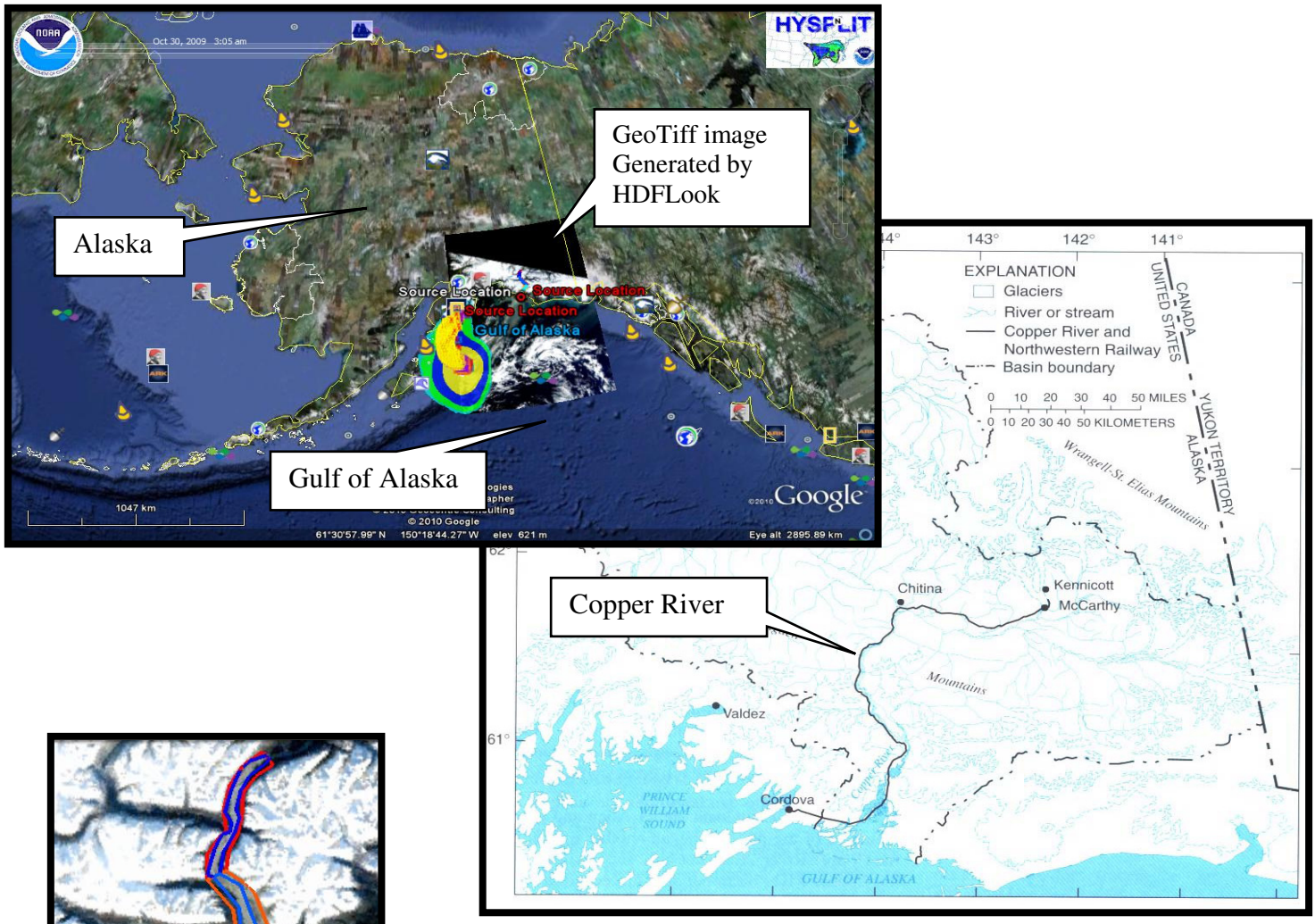

Figure 1a: Location of the Copper River Valley study site in south Alaska.

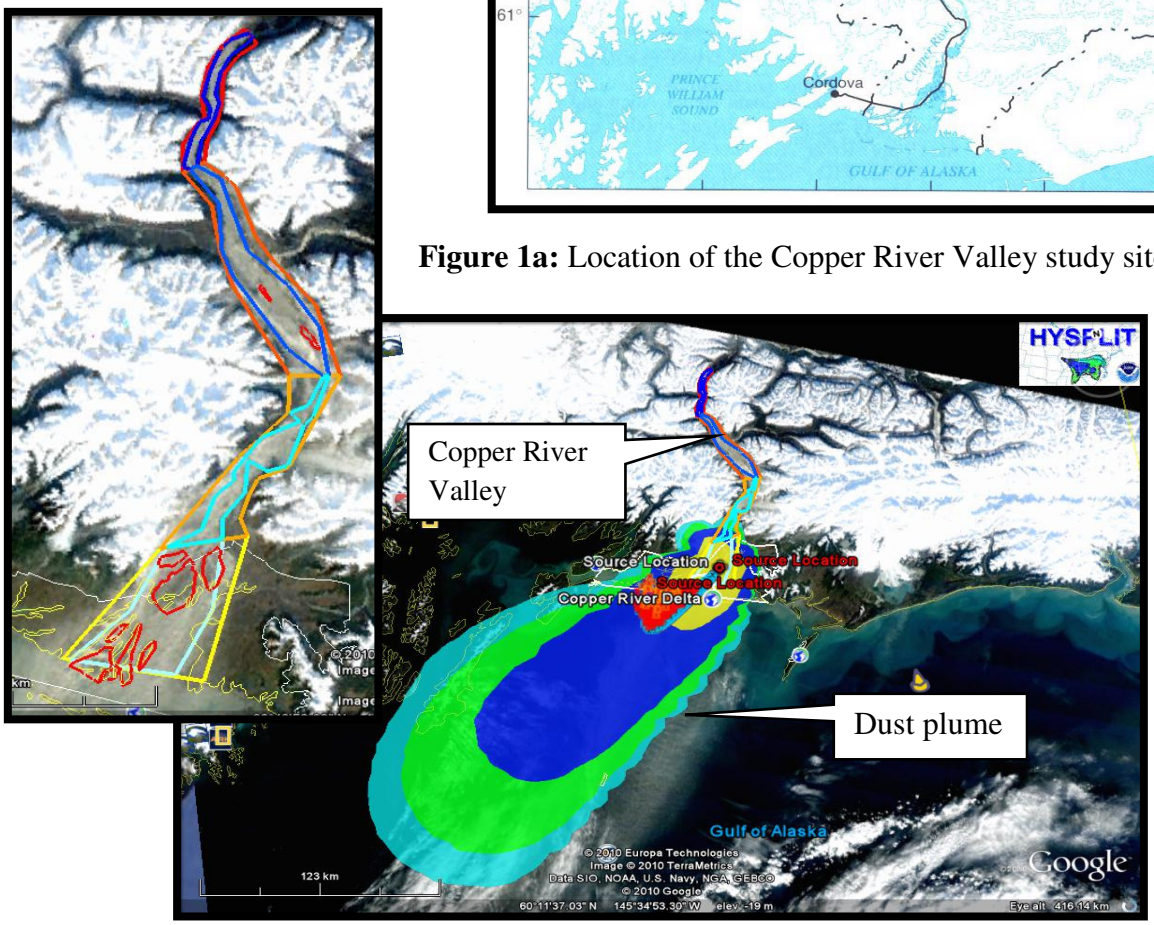

Figure 1b: Enlarged view of the Copper River Valley.

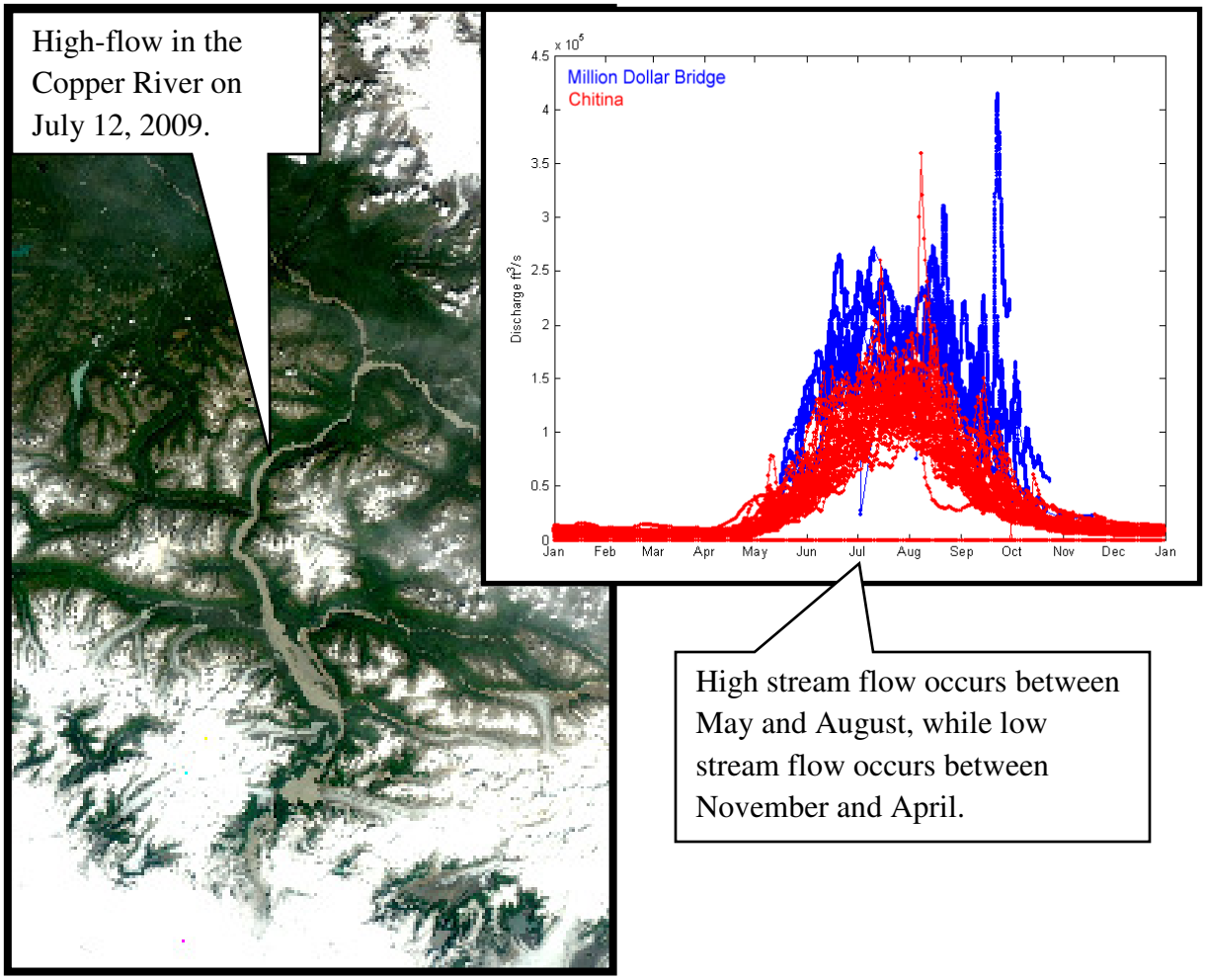

Figure 2a: MODIS satellite RGB (red, green, and blue) image of the Copper River during a high-flow period 2110 UTC 193 2009.

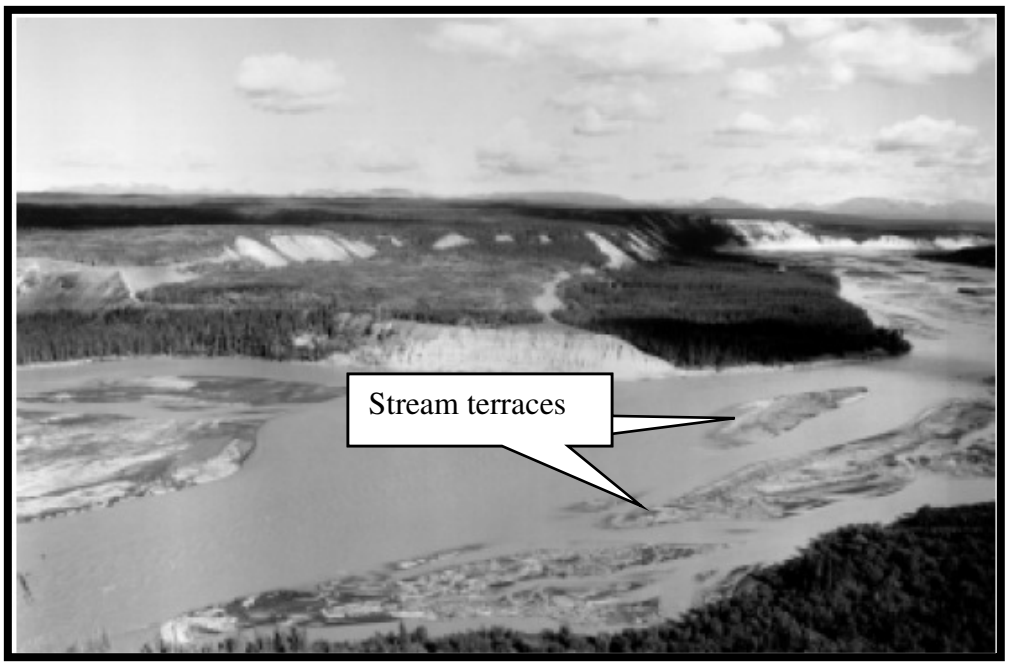

Figure 2b: Copper River stream terraces are formed by erosion of alluvial deposits.

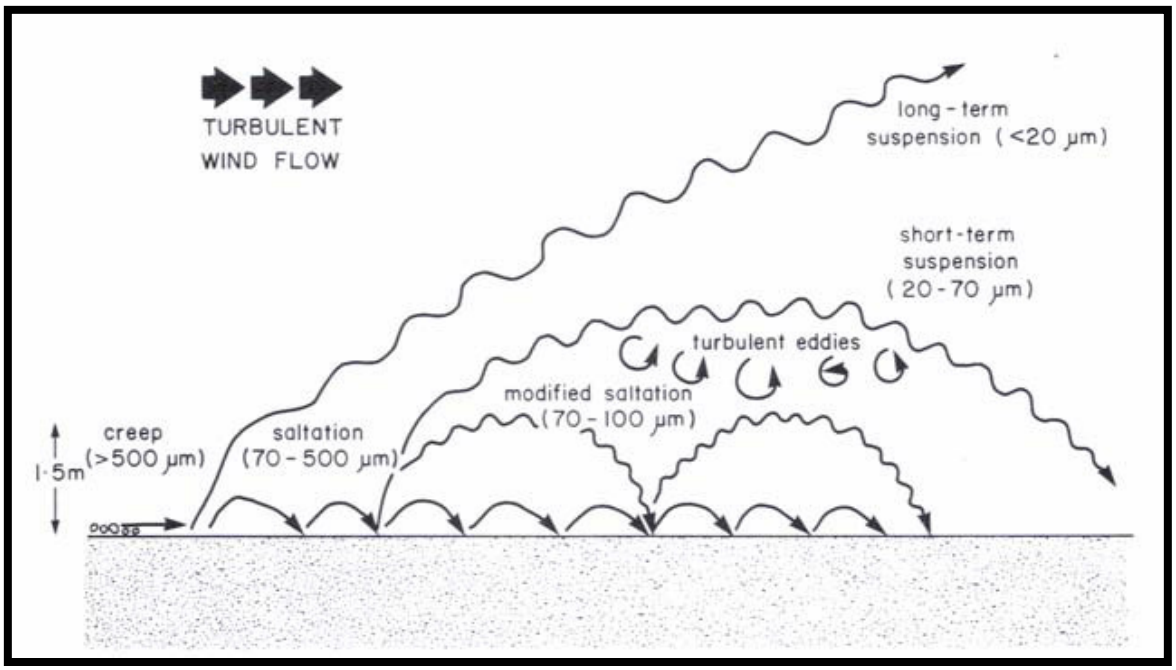

Figure 3: Particle transport modes with ranges of particle sizes (Pye, 1987).

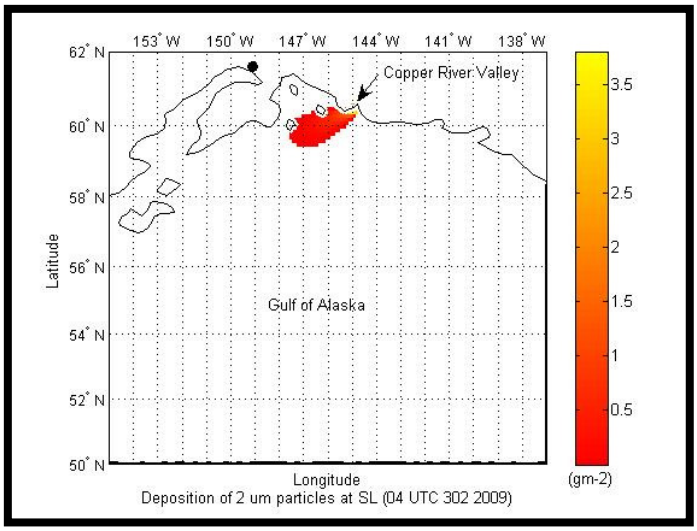

Figure 4: Dust deposition (gm^{-2}) area at sea-level (SL) at 0400 UTC 302 2009.

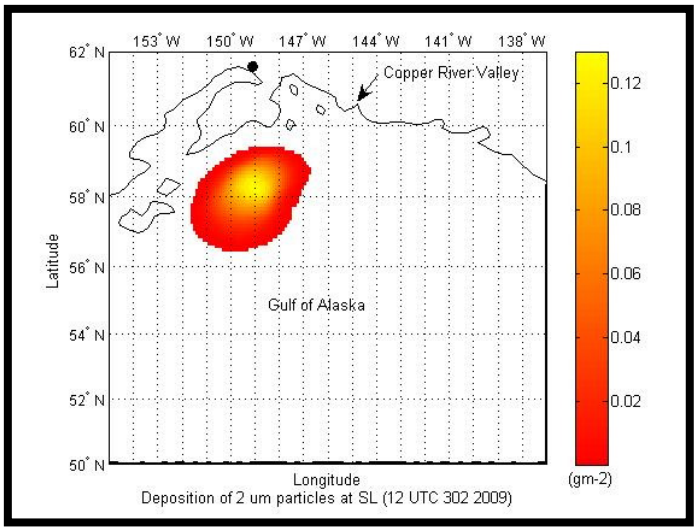

Figure 6: Dust deposition (gm^{-2}) area at sea-level (SL) at 1200 UTC 302 2009.

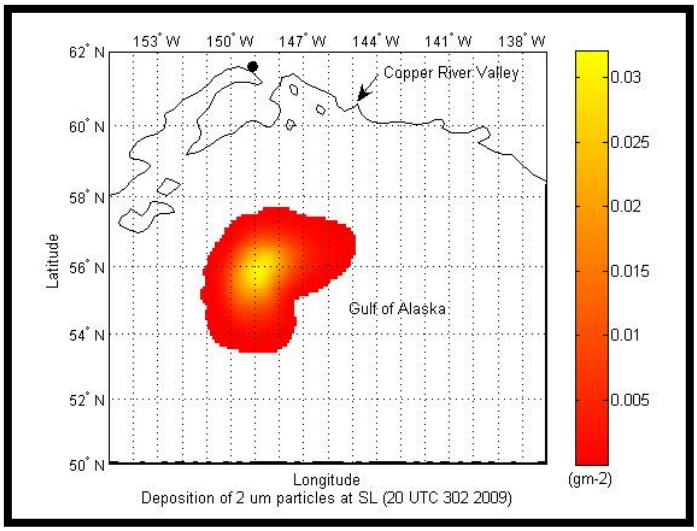

Figure 8: Dust deposition (gm^{-2}) area at sea-level (SL) at 2000 UTC 302 2009.

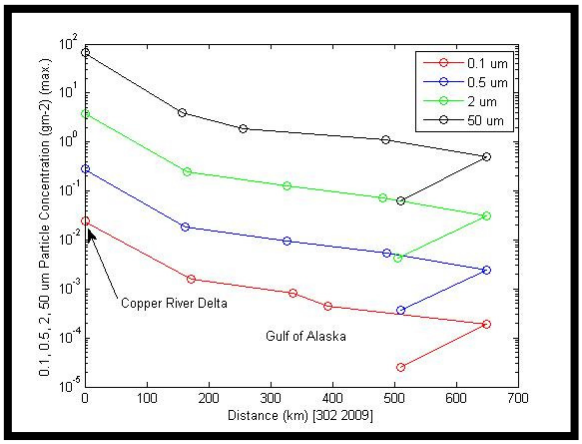

Figure 5: Concentration (gm^{-2}) versus transport distance (km) of 0.1, 0.5, 2, 50 μm size particles from 0000 to 2000 UTC 302 2009. Maximum concentration refers to the highest concentration value in the dust deposition area every 4 hours.

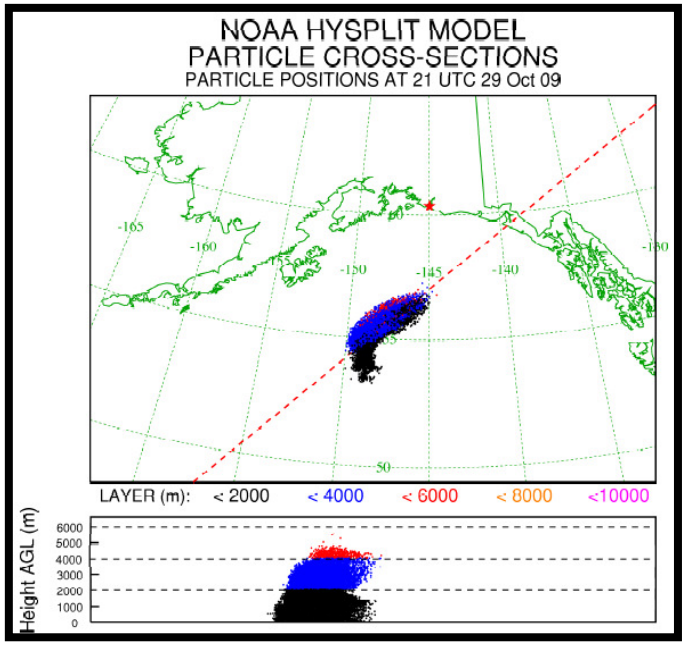

Figure 7: Particle position and AGL (above ground level) height (m) cross-section at 2100 UTC 302 2009.

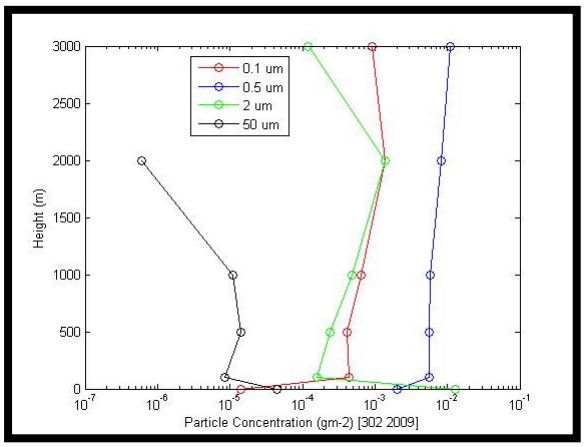

Figure 9: AGL (above ground level) height (m) versus concentration (gm^{-2}) of 0.1, 0.5, 2, 50 μm size particles at 2000 UTC 302 2009.

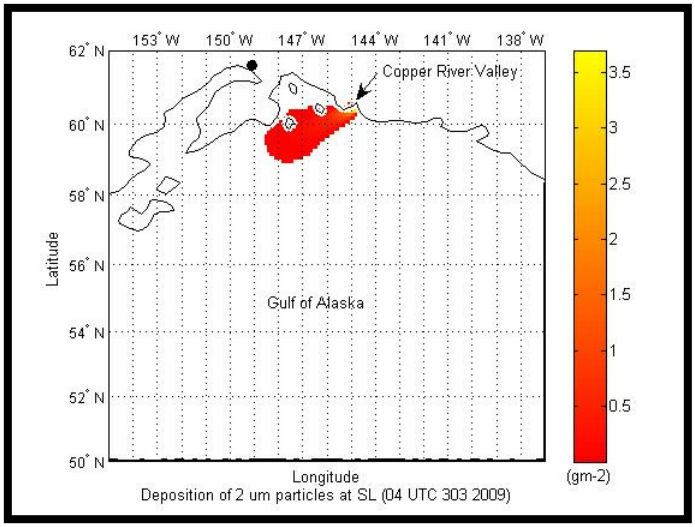

Figure 10: Dust deposition (gm^{-2}) area at sea-level (SL) at 0400 UTC 303 2009.

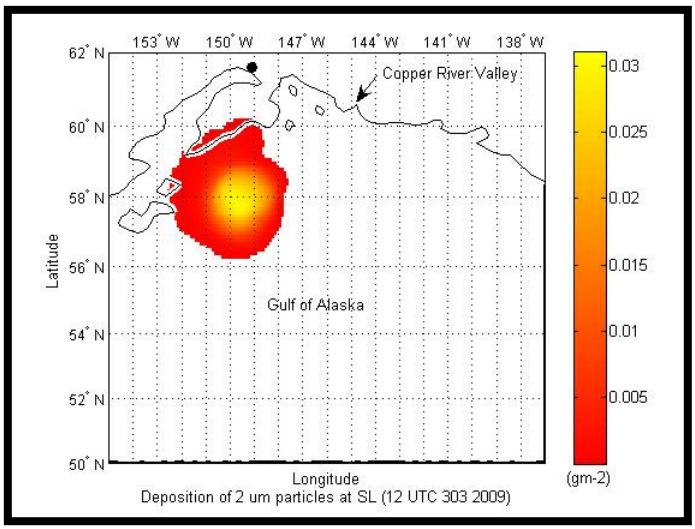

Figure 12: Dust deposition (gm^{-2}) area at sea-level (SL) at 1200 UTC 303 2009.

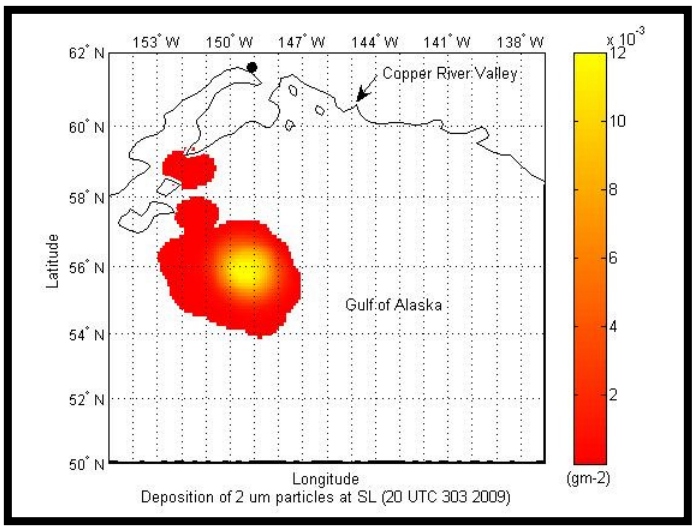

Figure 14: Dust deposition (gm^{-2}) area at sea-level (SL) at 2000 UTC 303 2009.

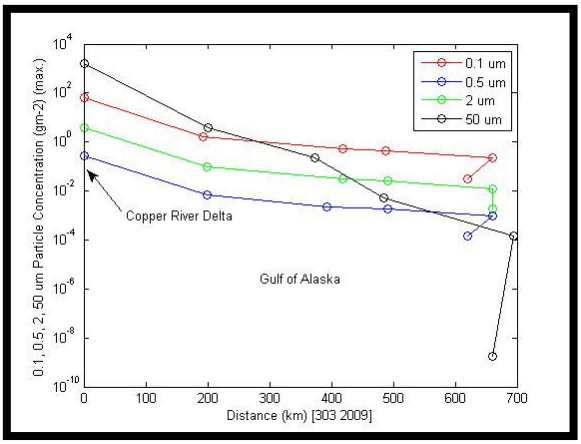

Figure 11: Concentration (gm^{-2}) versus transport distance (km) of 0.1, 0.5, 2, 50 μm size particles from 0000 to 2000 UTC 303 2009. Maximum concentration refers to the highest concentration value in the dust deposition area every 4 hours.

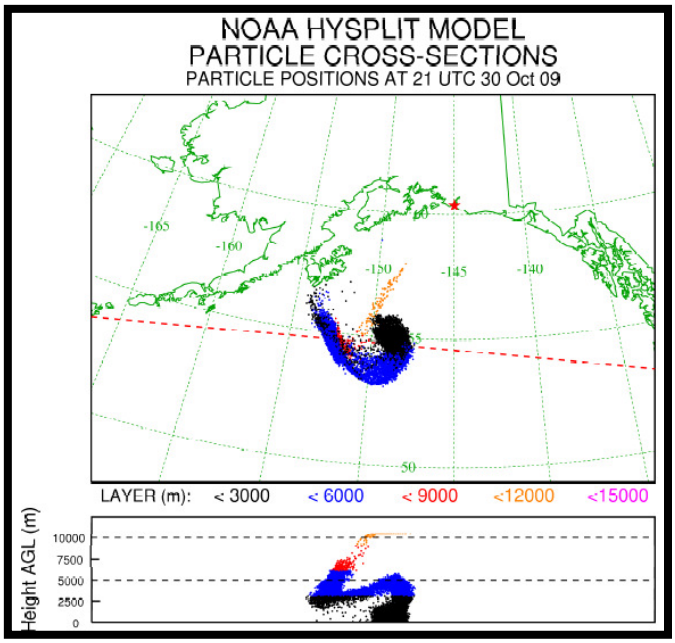

Figure 13: Particle position and AGL (above ground level) height (m) cross-section at 2100 UTC 303 2009.

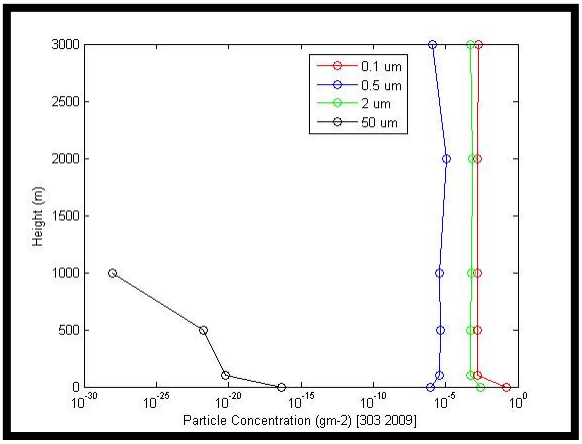

Figure 15: AGL (above ground level) height (m) versus concentration (gm^{-2}) of 0.1, 0.5, 2, 50 μm size particles at 2000 UTC 303 2009.

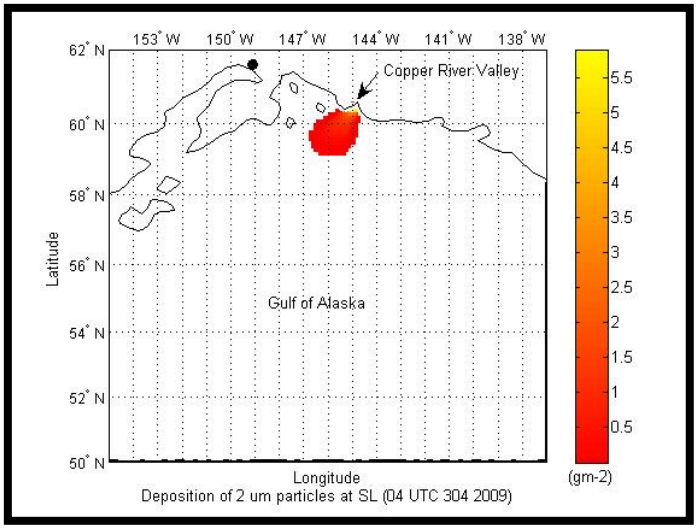

Figure 16: Dust deposition (gm^{-2}) area at sea-level (SL) at 0400 UTC 304 2009.

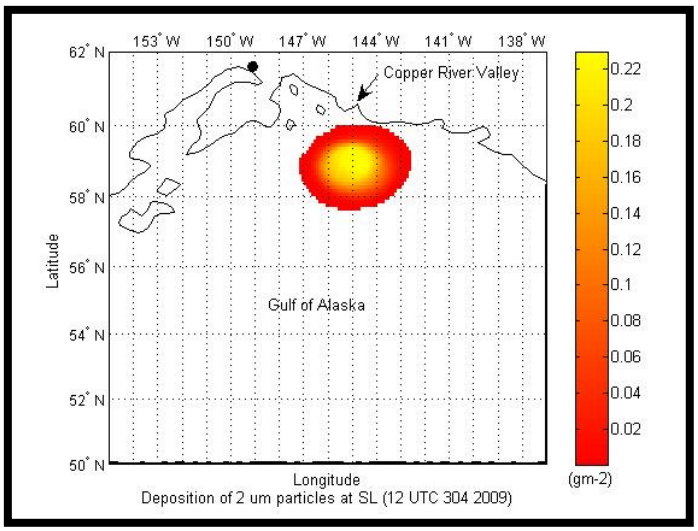

Figure 18: Dust deposition (gm^{-2}) area at sea-level (SL) at 1200 UTC 304 2009.

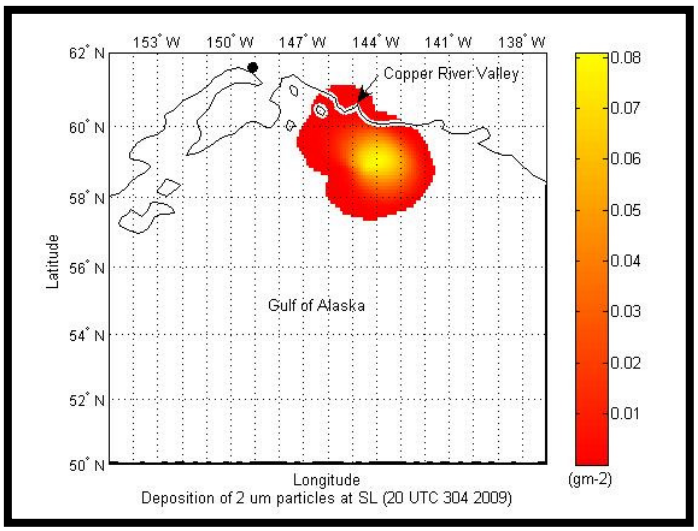

Figure 20: Dust deposition (gm^{-2}) area at sea-level (SL) at 2000 UTC 304 2009.

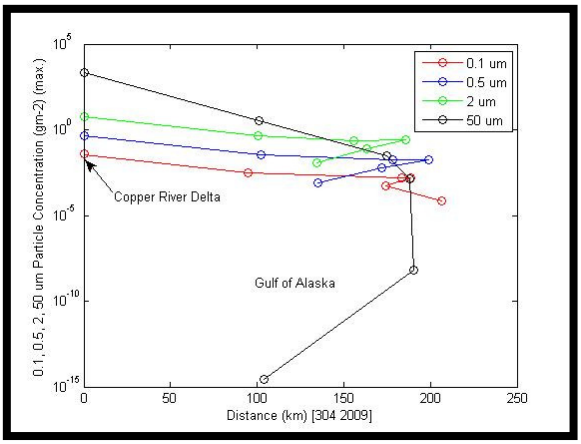

Figure 17: Concentration (gm^{-2}) versus transport distance (km) of 0.1, 0.5, 2, 50 μm size particles from 0000 to 2000 UTC 304 2009. Maximum concentration refers to the highest concentration value in the dust deposition area every 4 hours.

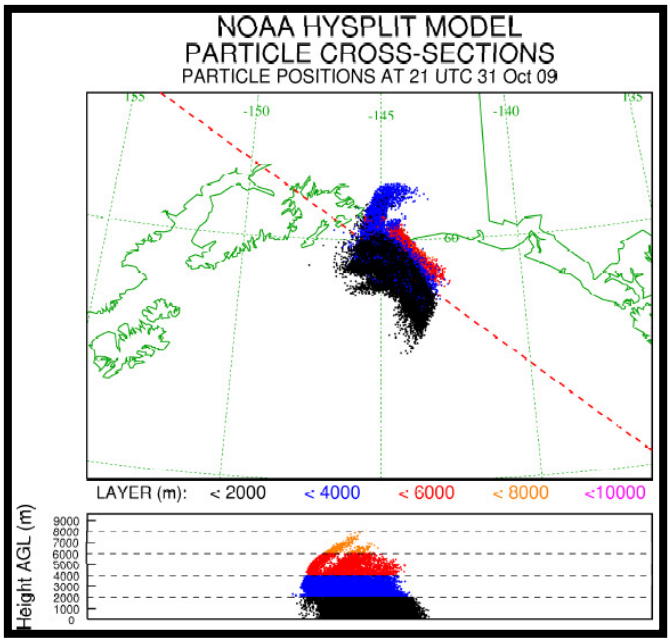

Figure 19: Particle position and AGL (above ground level) height (m) cross-section at 2100 UTC 304 2009.

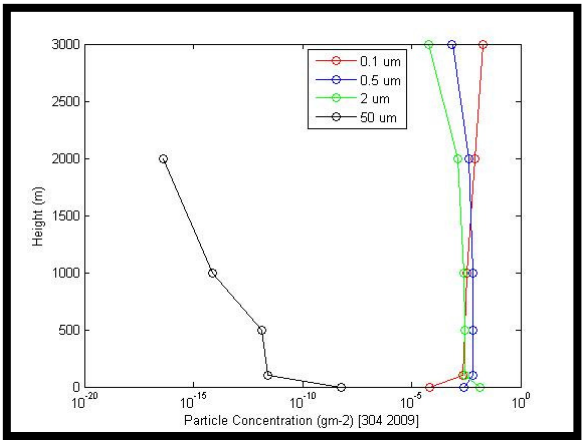

Figure 21: AGL (above ground level) height (m) versus concentration (gm^{-2}) of 0.1, 0.5, 2, 50 μm size particles at 2000 UTC 304 2009.

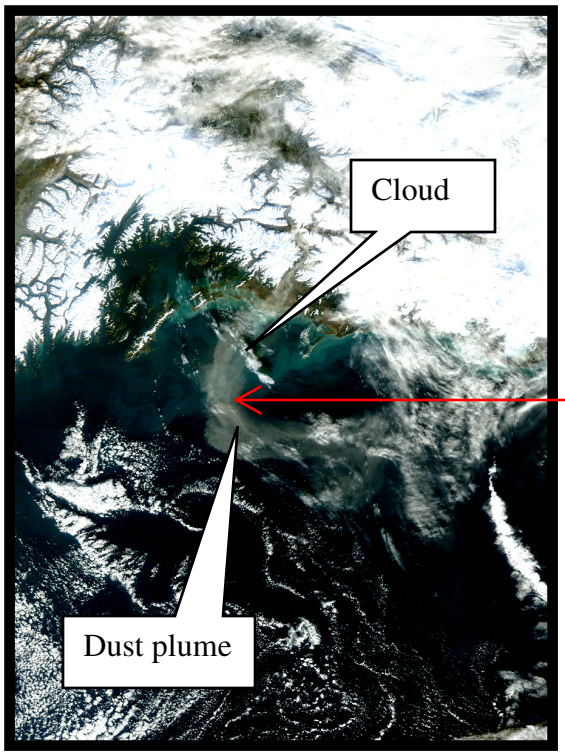

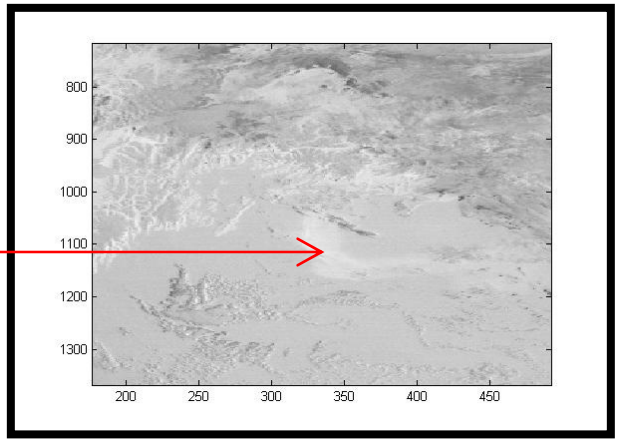

Figure 22: MODIS satellite RGB (red, green, and blue) image of a dust event in the Copper River Valley area at 2040 UTC 302 2009.

Figure 23: MODIS satellite grayscale image (HDF file processed by MATLAB) at 2125 UTC 303 2009. Note the cloud over the dust plume.

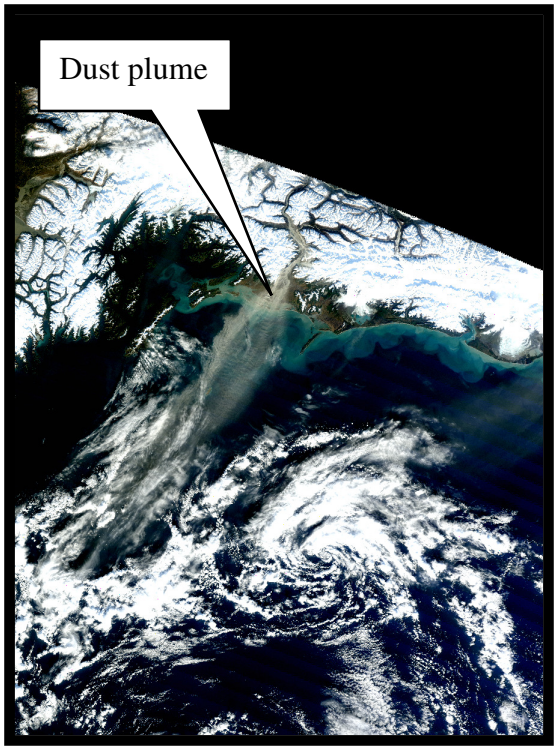

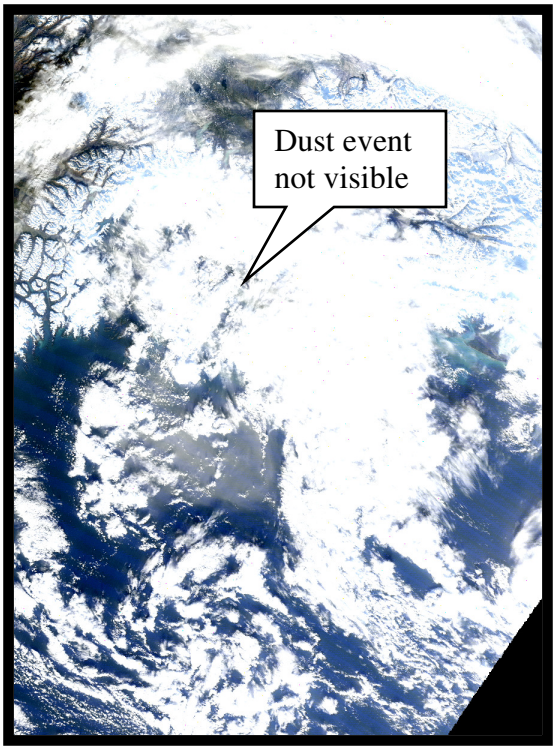

Figure 24: MODIS satellite RGB (red, green, and blue) image of a dust event in the Copper River Valley area at 2125 UTC 303 2009.

Figure 25: MODIS satellite RGB (red, green, and blue) image of Copper River Delta area at 2205 UTC 304 2009.

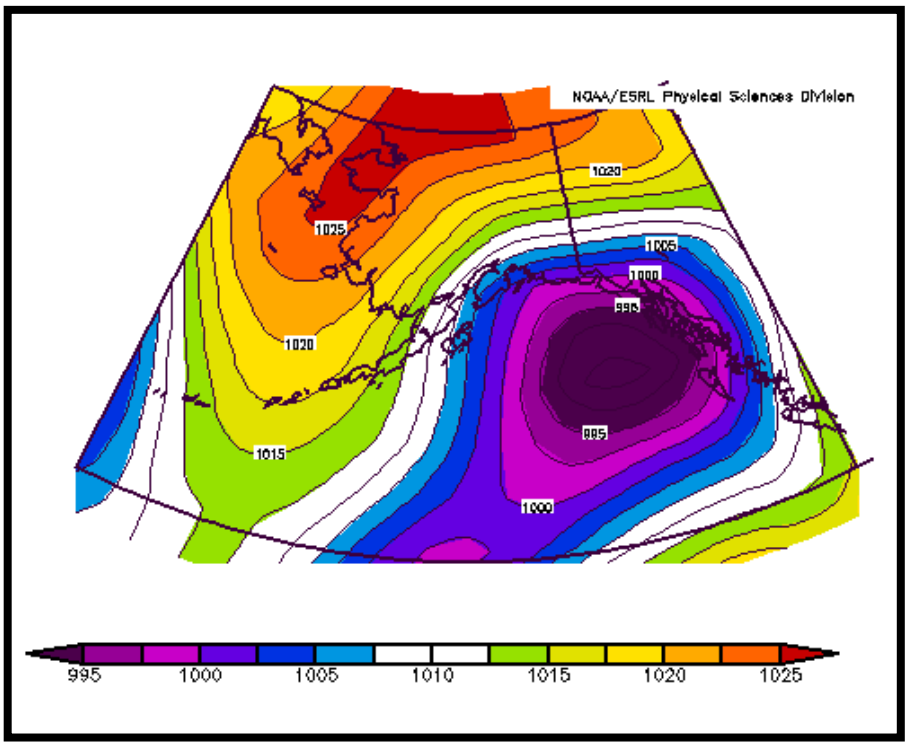

Figure 26: Mean sea-level pressure (mb) over Gulf of Alaska on 10/29/09.

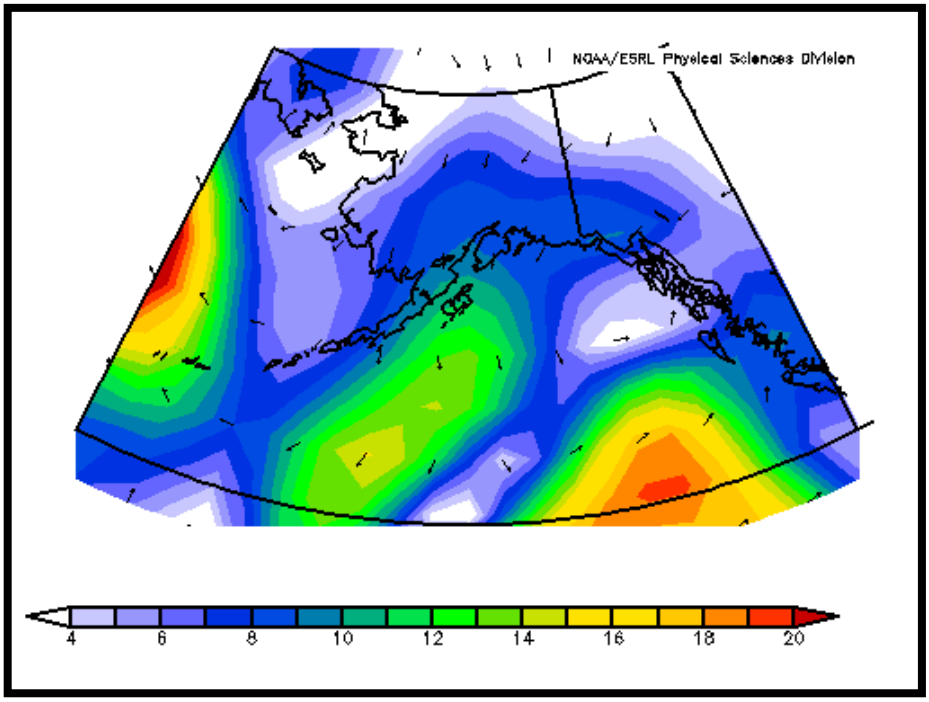

Figure 27: Mean wind velocity vectors (ms^{-1}) over Gulf of Alaska on 10/29/09.

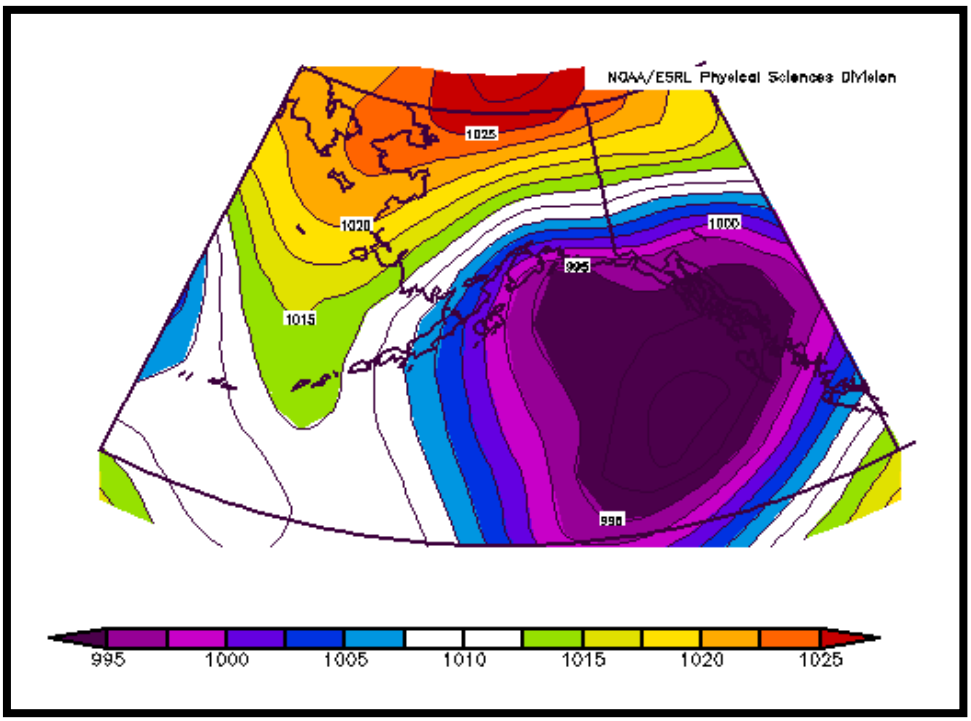

Figure 28: Mean sea-level pressure (mb) over Gulf of Alaska on 10/30/09.

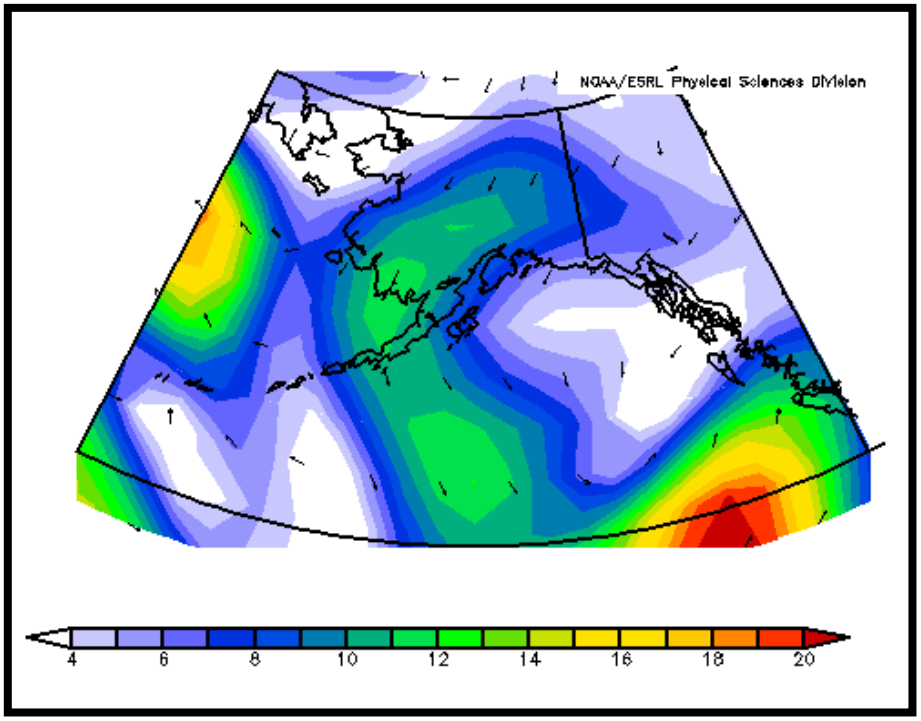

Figure 29: Mean wind velocity vectors (ms^{-1}) over Gulf of Alaska on 10/30/09.

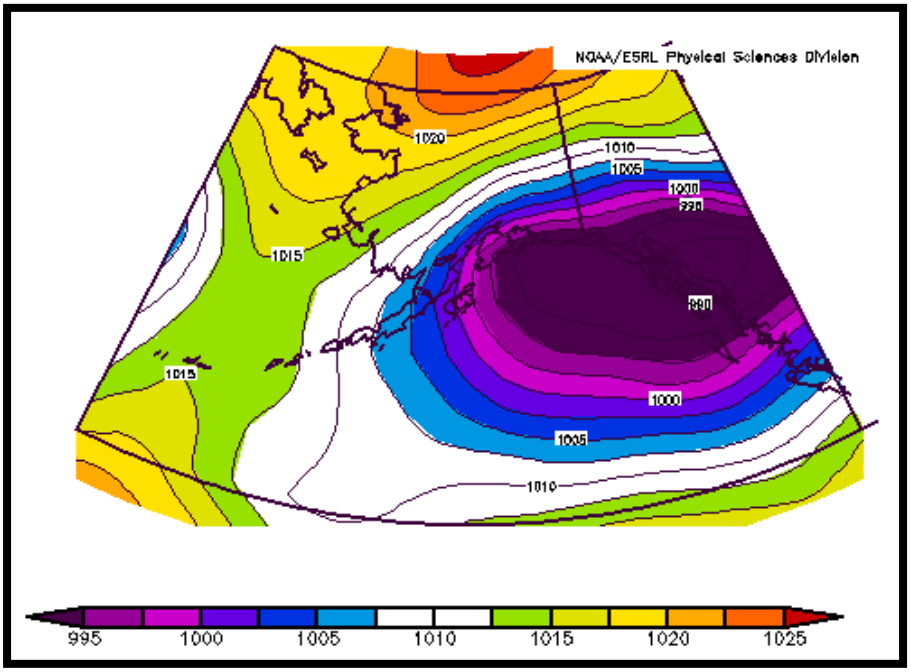

Figure 30: Mean sea-level pressure (mb) over Gulf of Alaska on 10/31/09.

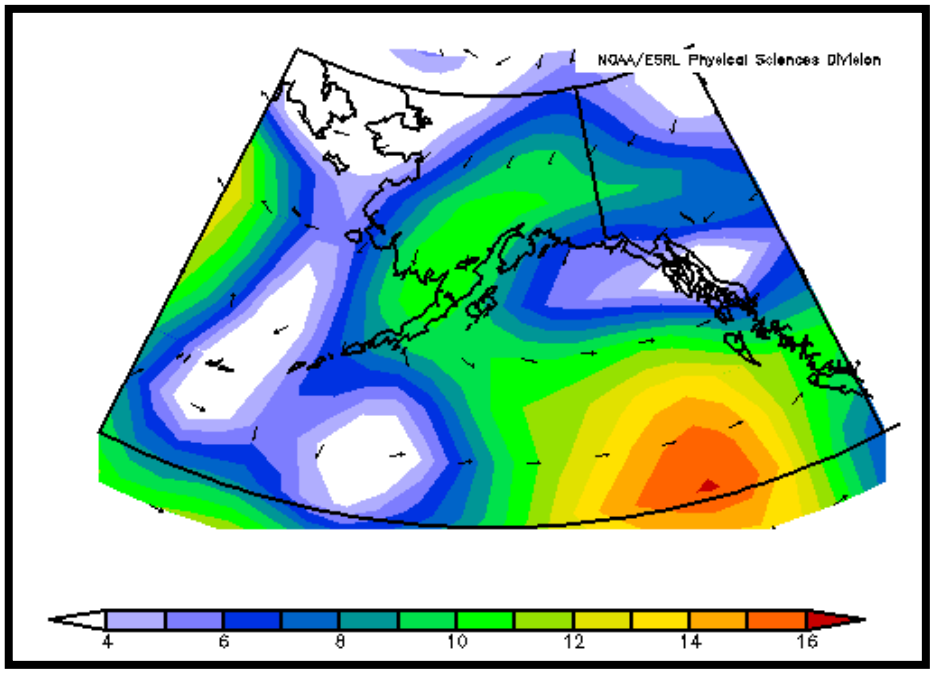

Figure 31: Mean wind velocity vectors (ms^{-1}) over Gulf of Alaska on 10/31/09.

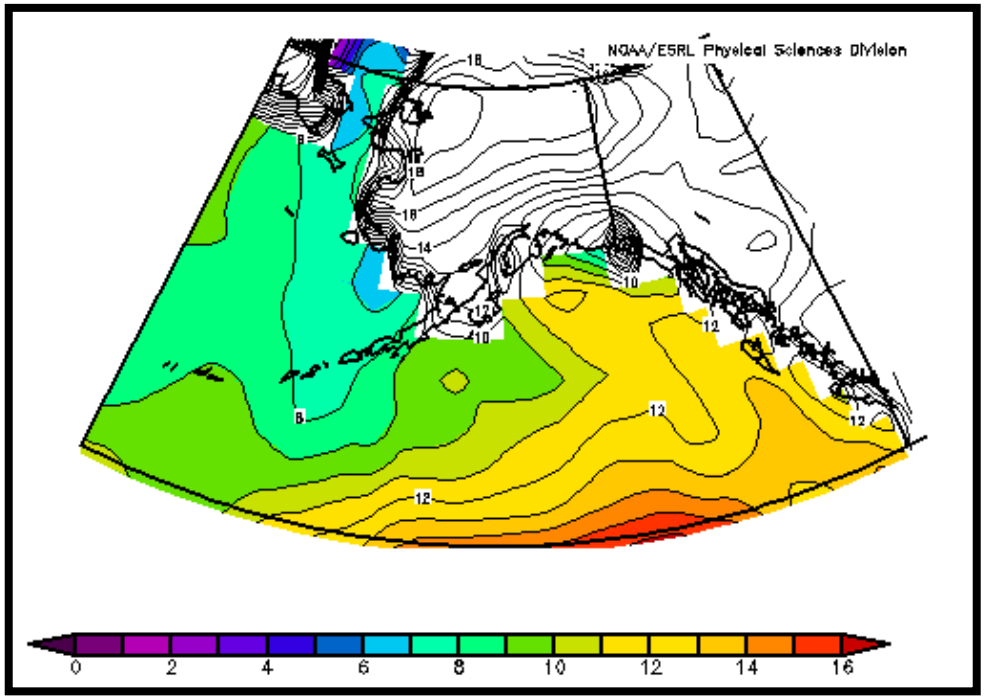

Figure 32: Mean sea surface temperatures (°C) over Gulf of Alaska were consistent between 10/29/09 - 10/31/09.

Table 1: Distance, height, and concentration results for a 2 μm particle on October 29, 2009.

2 μm ϕ Particle Data [October 29, 2009 (Julian Date 302)]			
Time (UTC)	Distance from source (km)	AGL height (m)	Concentration (gm^{-2})
0400	165	~1,500-2,000	2.5E-1
1200	482	~2,000-3,000	7.3E-2
2000	506	~4,500-5,000	4.3E-3

Table 2: Distance, height, and concentration results for a 2 μm particle on October 30, 2009.

2 μm ϕ Particle Data [October 30, 2009 (Julian Date 303)]			
Time (UTC)	Distance from source (km)	AGL height (m)	Concentration (gm^{-2})
0400	200	~3,500 – 4,500	3.7
1200	491	~5,500-7,500	2.6E-2
2000	661	~10,000	1.9E-3

Table 3: Distance, height, and concentration results for a 2 μm particle on October 31, 2009.

2 μm ϕ Particle Data [October 31, 2009 (Julian Date 304)]			
Time (UTC)	Distance from source (km)	AGL height (m)	Concentration (gm^{-2})
0400	101	~2,000-2,500	5.9
1200	186	~3,000-4,000	2.5E-1
2000	134	~6,000-8,000	1.1E-2

Table 4: Meteorological fields contained in the Global Data Assimilation System (GDAS) meteorological files.

Field	Units	Label	Data Order
Pressure at surface	hPa	PRSS	S1
Pressure reduced to mean sea level	hPa	MSLP	S2
Accumulated precipitation (6 h accumulation)	m	TPP6	S3
u-component of momentum flux (3- or 6-h average)	N/m2	UMOF	S4
v-component of momentum flux (3- or 6-h average)	N/m2	VMOF	S5
Sensible heat net flux at surface (3- or 6-h average)	W/m2	SHTF	S6
Downward short wave radiation flux (3- or 6-h average)	W/m2	DSWF	S7
Relative Humidity at 2m AGL	%	RH2M	S8
U-component of wind at 10 m AGL	m/s	U10M	S9
V-component of wind at 10 m AGL	m/s	V10M	S10
Temperature at 2m AGL	K	TO2M	S11
Total cloud cover (3- or 6-h average)	%	TCLD	S12
Geopotential height (units in geopotential meters)	gpm	SHGT	S13
Convective available potential energy	J/Kg	CAPE	S14
Convective inhibition	J/kg	CINH	S15
Standard lifted index	K	LISD	S16
Best 4-layer lifted index	K	LIB4	S17
Planetary boundary layer height	m	PBLH	S18
Temperature at surface	K	TMPS	S19
Accumulated convective precipitation (6 h accumulation)	m	CPP6	S20
Volumetric soil moisture content	frac.	SOLM	S21
Categorial snow (yes=1, no=0) (3- or 6-h average)		CSNO	S22
Categorial ice (yes=1, no=0) (3- or 6-h average)		CICE	S23
Categorial freezing rain (yes=1, no=0) (3- or 6-h average)		CFZR	S24
Categorial rain (yes=1, no=0) (3- or 6-h average)		CRAI	S25
Latent heat net flux at surface (3- or 6-h average)	W/m2	LHTF	S26
Low cloud cover (3- or 6-h average)	%	LCLD	S27
Middle cloud cover (3- or 6-h average)	%	MCLD	S28
High cloud cover (3- or 6-h average)	%	HCLD	S29
Geopotential height	gpm*	HGTS	U1
Temperature	K	TEMP	U2
U-component of wind with respect to grid	m/s	UWND	U3
V-component of wind with respect to grid	m/s	VWND	U4
Pressure vertical velocity	hPa/s	WWND	U5
Relative humidity	%	RELH	U6

References

Ackerman, S. A., Strabala, K. I., Menzel, W. P., Frey, R. A., Moeller, C. C., and Gumley, L.E., 1998. Discriminating clear-sky from clouds with MODIS. J. Geophys. Res., 103 (D24), 32 141-32 157.

Bagnold, R. A., 1941. The Physics of Blown Sand and Desert Dunes, Methuen, London. 241pp.

Bagnold, R. A., 1954. The Physics of Blown Sand and Desert Dunes, Dover, New York, pp. 1-6, 85-95.

Bowersox, R., 2002. "Hydrology of a glacial dominated system, Copper River, Alaska." Glacial and Periglacial Processes as Hydrogeomorphic and Ecological Drivers in High-Latitude Watersheds. Eds. J. Mount, P. Moyle and S. Yarnell. Davis, California, 1-7. (Available over the internet at http://watershed.ucdavis.edu/copper_river/background/data/BowersoxCopper.pdf) Retrieved July 8, 2010.

Carrick, S., 1992. Copper River Highway environmental impact studies: hydrological aspects. Fairbanks, Alaska, State of Alaska, Department of Natural Resources, Division of Geological and Geophysical Surveys.

Clark, M.H., and Kautz, D.R., 1990. Soil Survey for Copper River Area, Alaska. United States Department of Agriculture, Soil Conservation Service. U.S. Gov't Printing Off. pp. 278. (Available over the internet at http://soildatamart.nrcs.usda.gov/Manuscripts/AK612/0/CopperRiver.pdf) Retrieved July 7, 2010.

Draxler, R. R., Gillette, D. A., Kirkpatrick, J. S., and Heller J., 2001. Estimating PM10 air concentrations from dust storms in Iraq, Kuwait, and Saudi Arabia, Atmos. Environ., 35, 4315-4330.

Eby, G.N., 2004. Principles of Environmental Geochemistry. Brooks/Cole - Thomson Learning, Inc., Pacific Grove, California, pp. 289-290, 412-415.

Escudero, M., Stein, A., Draxler, R.R., Querol, X., Alastuey, A., Castillo, S., and Avila, A., 2006. Determination of the contribution of northern Africa dust source areas to PM10 concentrations over the central Iberian Peninsula using the Hybrid Single-Particle Lagrangian Integrated Trajectory model HYSPLIT model. Journal of Geophysical Research, Vol. 111, D06210, doi:10.1029/2005JD006395.

Frey, R.A., Ackerman, S.A., Liu, Y., Strabala, K.I., Zhang, H., Key, J.R., and Wang, X., 2008. Cloud Detection with MODIS. Part I: Improvements in the MODIS Cloud Mask for Collection 5. J. Atmos. Oceanic Technol., 25, 1057-1072.

Fryrear, D.W., and Saleh, A., 1993. Field wind erosion: vertical distribution. Soil Science 155, 294-300.

Goossens, D., 2005. Quantification of the dry aeolian deposition of dust on horizontal surfaces: an experimental comparison of theory and measurements, Sedimentology, 52, 859-873.

Hao, X., and Qu, J.J., 2007. Saharan dust storm detection using MODIS thermal infrared bands. Journal of Applied Remote Sensing, Vol. 1, 013510.

Kuss, J., and Kremling, K., 1999. Spatial variability of particle associated trace elements in near –surface waters of the North Atlantic (30°N/60°W to 60°N/2°W), derived by large volume sampling. Marine Chemistry 68, 71-86.

Libes, S.M., 1992. An Introduction to Marine Biogeochemistry. New York: John Wiley & Sons, pp. 734.

Lillesand, T.M., Kiefer, R.W., and Chipman, J.W., 2004. Remote Sensing and Image Interpretation, 3rd ed. New York: John Wiley & Sons, pp. 1-26, 478-480, 545-550.

Marvill, S., and Jayaweera, K., 1975. Investigations of Strong Valley Winds in Alaska using Satellite Infrared Imagery. Monthly Weather Review, Vol. 103, No. 12, 1129-1136.

Prandtl, L., 1935. The mechanics of viscous fluids. In F. Durand (ed.) Aerodynamic Theory, Vol. III. Julius Springer, Berlin, pp. 57-109.

Pye, K., 1987. Aeolian Dust and Dust Deposits. Academic Press, London, pp. 29-62.

Seinfeld, J. H., and Pandis, S. N., 1998. Atmospheric Chemistry and Physics: From Air Pollution to Climate Change. Wiley-Interscience, New York, New York, pp. 462-468, 1193-1208.

U.S. Department of Agriculture (USDA), Soil Survey Staff, Natural Resources Conservation Service, National Soil Survey Handbook, Title 430-VI, U.S. Government Printing Office, Washington, DC, 1997. (Available over the internet at http://www.soils.usda.gov.)

Van der Hoven, I., 1968. Deposition of particles and gases. In Meteorology and Atomic Energy. D. Slade (Ed.), TID-24190, NTIS, Springfield, VA, 445 pp.

von Kármán, T., 1934. Turbulence and skin friction. Journal of the Aeronautical Sciences 1, 1-20.

Wallace, J.M., and Hobbs, P.V., 2006. Atmospheric science: An introductory survey, Academic Press, New York, pp. 404-407.

Westphal, D. L., Toon, O.B., and Carlson, T.N., 1987. A two-dimensional numerical investigation of the dynamics and microphysics of Saharan dust storms, J. Geophys. Res., 92(D3), 3027 - 3049.